

Graphene-based Li-ion hybrid supercapacitors with ultrahigh performance

Kai Leng, Fan Zhang, Long Zhang, Tengfei Zhang, Yingpeng Wu, Yanhong Lu, Yi Huang, and Yongsheng Chen (✉)

Key Laboratory of Functional Polymer Materials and Centre for Nanoscale Science and Technology, Institute of Polymer Chemistry, College of Chemistry, Nankai University, Tianjin300071, China

Received: 11 April 2013

Revised: 18 May 2013

Accepted: 19 May 2013

© Tsinghua University Press and Springer-Verlag Berlin Heidelberg 2013

KEYWORDS

graphene,
hybrid supercapacitor,
Li-ion battery,
supercapacitor

ABSTRACT

There is a growing demand for hybrid supercapacitor systems to overcome the energy density limitation of existing-generation electric double layer capacitors (EDLCs), leading to next generation-II supercapacitors with minimum sacrifice in power density and cycle life. Here, an advanced graphene-based hybrid system, consisting of a graphene-inserted $\text{Li}_4\text{Ti}_5\text{O}_{12}$ (LTO) composite anode (G-LTO) and a three-dimensional porous graphene-sucrose cathode, has been fabricated for the purpose of combining both the benefits of Li-ion batteries (energy source) and supercapacitors (power source). Graphene-based materials play a vital role in both electrodes in respect of the high performance of the hybrid supercapacitor. For example, compared with the theoretical capacity of $175 \text{ mA}\cdot\text{h}\cdot\text{g}^{-1}$ for pure LTO, the G-LTO nanocomposite delivered excellent reversible capacities of 207, 190, and $176 \text{ mA}\cdot\text{h}\cdot\text{g}^{-1}$ at rates of 0.3, 0.5, and 1 C, respectively, in the potential range 1.0–2.5 V vs. Li/Li^+ ; these are among the highest values for LTO-based nanocomposites at the same rates and potential range. Based on this, an optimized hybrid supercapacitor was fabricated following the standard industry procedure; this displayed an ultrahigh energy density of $95 \text{ Wh}\cdot\text{kg}^{-1}$ at a rate of 0.4 C (2.5 h) over a wide voltage range (0–3 V), and still retained an energy density of $32 \text{ Wh}\cdot\text{kg}^{-1}$ at a high rate of up to 100 C, equivalent to a full discharge in 36 s, which is exceptionally fast for hybrid supercapacitors. The excellent performance of this Li-ion hybrid supercapacitor indicates that graphene-based materials may indeed play a significant role in next-generation supercapacitors with excellent electrochemical performance.

1 Introduction

There is increasing interest in new energy storage technologies to meet the future challenges of high-

efficiency energy storage systems. Among these energy storage systems, electrochemical capacitors (ECs) and lithium-ion batteries (LIBs) are currently considered to be the most promising. Of many different kinds of ECs,

Address correspondence to yschen99@nankai.edu.cn

electric double layer capacitors (EDLCs) using carbon-based active materials, are the most common devices at present [1–3]. In comparison with EDLCs, LIBs can provide higher energy densities (150–200 Wh·kg⁻¹), but their power capabilities are relatively low. In contrast, EDLCs exhibit competitive advantages such as the highest known power capability (2–5 kW·kg⁻¹) and long cycle life [4–7]. However, the low energy densities of these traditional generation-I EDLCs have limited their use in high energy density storage devices. To overcome the energy density limitation, new energy devices with hybrid characteristics, considered as generation-II supercapacitors, are strongly desired [8]. In recent years, hybrid supercapacitor systems with a battery-like electrode (energy source) and a capacitor-like electrode (power source) have been widely reported [9–13]. In 2001, Amatucci et al. were the first to report a non-aqueous hybrid system with a high energy density exceeding 10 Wh·kg⁻¹, which consisted of a lithium titanate (Li₄Ti₅O₁₂, LTO) anode and an activated carbon (AC) cathode [14]. Following this pioneering work, numerous hybrid systems have been studied. For example, a hybrid AC/LiPF₆/Li₄Ti₅O₁₂-C cell [15] demonstrated an energy density of 20 Wh·kg⁻¹; a CNT/LiPF₆/TiO₂-B [16] supercapacitor showed an energy density of 12.5 Wh·kg⁻¹ at a rate of 10 C over a voltage region of 0–2.8 V; a hybrid spinel-LiMn₂O₄/LiClO₄/AC cell [17] has been reported to show an energy density of 45 ± 5 Wh·kg⁻¹ at 0.03 kW·kg⁻¹; Ni-doped spinel-LiMn₂O₄ hybrid cell configurations such as LiNi_{0.5}Mn_{1.5}O₄/LiPF₆/AC [18] exhibited voltages higher than 4.7 V and an energy density of 55 Wh·kg⁻¹. Hybrid supercapacitors can provide a maximum operating voltage by taking full advantages of the different potential ranges of the two electrodes, which leads to large increases in energy density [19]. The overall goals of these generation-II hybrid supercapacitor systems are to increase the energy density with the minimum sacrifice in power capability and cycle life for deep discharges [8, 9].

Overall, designing outstanding electrode materials is still the biggest challenge to realizing the desired performance [20]. Studies of the design of high capacitance supercapacitors as a capacitor-type electrode in hybrid energy storage systems have mainly focused on introducing new materials with high specific surface

area (SSA) and high electrical conductivity [21, 22]. In contrast, the cycle performance of hybrid supercapacitors is significantly decreased by the poor reversible stability of battery-type electrodes. Therefore, negative electrodes with structural stability, higher energy density, and rapid charging/discharging should be developed. So far, many different kinds of transition metal oxides, lithium metal alloys and TiO₂-B nanowire materials have been investigated extensively as LIB electrodes [23–26]. Recently, Naoi et al. reported a hybrid supercapacitor system utilizing an ultrafast negative electrode based on nanoscale LTO/carbon nanofibers. The authors noted that LTO is a stable and safe redox material capable of increasing the energy density of hybrid supercapacitors without sacrificing the interfacial characteristics [27, 28]. LTO has the advantages of high theoretical capacity (175 mA·h·g⁻¹), high Coulombic efficiency (close to 100%), a stable 1.55 V operating voltage versus Li/Li⁺, and zero-strain structure characteristics with no formation of a solid electrolyte interface (SEI) film. These advantages make it a highly promising anode material for LIBs [29–32]. However, LTO has inherently low electronic conductivity, which seriously limits its high rate capability [33, 34]. Inspired by the potential applications of LTO, numerous efforts have been devoted to enhance its conductivity by measures such as reducing particle size, designing special nanostructures, and doping with aliovalent metal ions [35–38]. Recently, coating LTO with conductive carbonaceous materials such as thin carbon layers or carbon nanofibers and carbon nanotubes, has also been shown to be an effective way to significantly improve the performance [39, 40].

Graphene, with its extraordinary properties such as high surface area, ultrahigh electrical conductivity and excellent mechanical flexibility, has become one of the most appealing conductive carbon matrices for nanostructured hybrid electrodes [41, 42]. More importantly, the 3D interconnected porous graphene network prepared through hydrothermal and solvothermal reduction methods gives the material good mechanical strength and flexibility, which makes it an ideal material for fabricating composite anode materials with metal oxides [43, 44]. Here, we report that LTO can be directly anchored on conducting graphene nanosheets (GNS) formed by reduction of

graphene oxide (GO) in a practical and easy approach using direct solvothermal and heat treatment steps. The nanostructure of the graphene–LTO (G–LTO) anode endows the composites with larger reversible capacities compared with the theoretical capacity ($175 \text{ mA}\cdot\text{h}\cdot\text{g}^{-1}$) of pure LTO at low rates, and enhanced rate capability. Moreover, when combined with a graphene-enhanced high performance graphene–sucrose (G–SU) cathode, the resulting optimized hybrid supercapacitor shows high energy densities in the range $95\text{--}32 \text{ Wh}\cdot\text{kg}^{-1}$ (according to an industry standard based on the total mass of active electrode materials) in the potential range of 0–3 V over rates from 0.4 to 100 C (where 1 C represents complete discharge in 1 h).

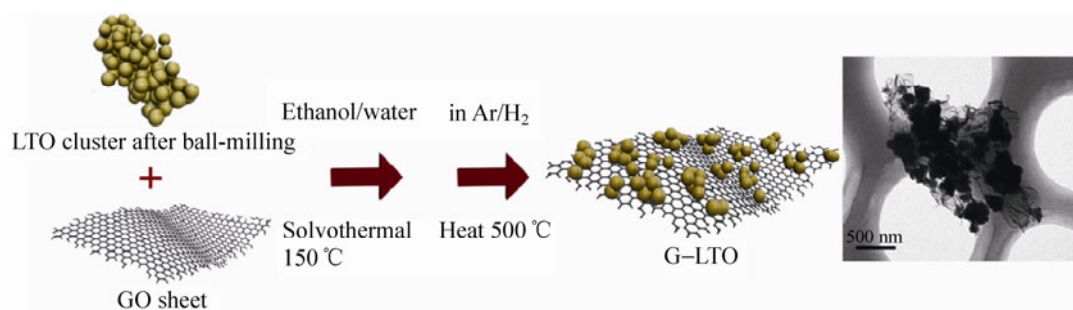
2 Results and discussion

2.1 Negative electrode materials

The G–LTO nanocomposite was fabricated by a process including solvothermal reaction of an ethanol/water-based colloidal suspension of LTO and GO and subsequent heat treatment (Scheme 1). Composites were synthesized with different ratios of GO and LTO, and the optimized product with only 3.6 wt.% of graphene (according to the thermogravimetric analysis, Fig. S1 in the Electronic Supplementary Material (ESM)) was selected as discussed below. LTO is expected to become homogeneously attached to the surface and edges of the GO sheets by virtue of the interaction between the functional groups on the GO sheets and LTO particles during solvothermal and heat treatment. Thus, the electrical network of graphene nanosheets should produce effective pathways for electron and ion transport, resulting in improved performance of the electrode. For example, the electrical conductivity

of the G–LTO nanocomposite was $\sim 0.04 \text{ S/m}$, as compared with a value of only 10^{-7} S/m for pure LTO [45]. Figure 1(a) shows the X-ray diffraction (XRD) profiles of the G–LTO nanocomposite and pure LTO, which reveal that all the peaks for the G–LTO nanocomposite are identical to those of pure LTO (JCPDS File No. 26-1198). It is worth noting that the characteristic peaks of graphene are not observed in the XRD pattern of the G–LTO nanocomposite, which indicates that graphene sheets present in the hybrid were distributed in a random and disordered pattern, suggesting they had no impact on the crystal structure of LTO.

Raman spectroscopy and X-ray photoelectron spectroscopy (XPS) were performed to further understand the interfacial interaction in the G–LTO nanocomposite. The Raman spectra of the LTO and G–LTO nanocomposite are shown in Fig. 1(b). The Raman spectrum of the G–LTO nanocomposite exhibits the typical peaks of commercial LTO, corresponding to the characteristic features of the spinel structure ($A_{1g} + E_g + 3F_{2u}$) [46], with two additional strong peaks at $1,350$ and $1,600 \text{ cm}^{-1}$, which are assigned [47] to the D-band and G-band of graphene, respectively. Figures 1(c) and S2 (in the ESM) show the XPS measurements for various elements on the G–LTO nanocomposite surface. The survey spectrum mainly shows peaks corresponding to Li 1s, Ti 2p, and O 1s due to the LTO phase, and C 1s due to the graphene sheets in the G–LTO nanocomposite. The C 1s peak at 284.8 eV is related to graphitic carbon in graphene. Moreover, the C 1s (286.9 eV) peak and the O 1s (532.5 eV) peak show that some residual oxygen-containing functionalities are still present on the reduced graphene oxide (RGO) sheets. The O 1s peak at 530.8 eV corresponds to O bonded to Ti in LTO. Elemental analyses by combustion and inductively coupled plasma mass



Scheme 1 Schematic illustration of the synthesis of G–LTO nanocomposite.

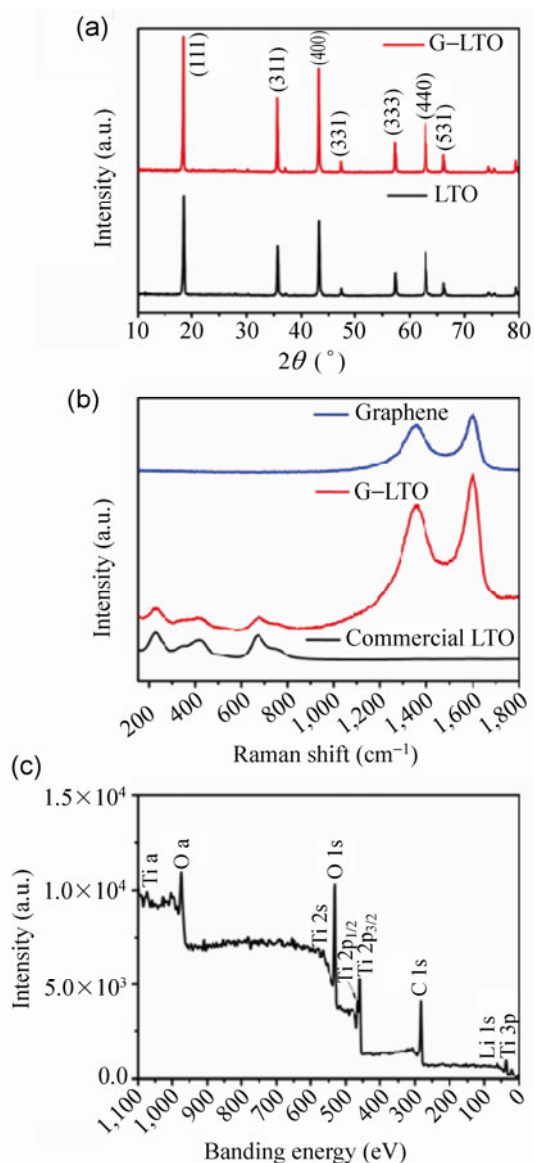


Figure 1 (a) XRD patterns of G-LTO nanocomposite and pure LTO particles. (b) Raman spectra of G-LTO nanocomposite, pristine graphene sheets and commercial LTO. (c) XPS spectrum of the G-LTO nanocomposite.

spectrometry (ICP-MS) show that the G-LTO consists of ~3.5 wt.% C (consistent with the thermogravimetric analysis), ~0.9 wt.% H, ~63.4 wt.% O, ~5.2 wt.% Li, and ~26.9 wt.% Ti.

The morphology the G-LTO nanocomposite was characterized by scanning electron microscopy (SEM) and transmission electron microscopy (TEM). It can be clearly observed from Figs. 2(a)–2(c) that LTO particles with a size of 100–500 nm are well dispersed among the crumpled graphene network with a low degree of agglomeration. The solvothermal treatment ensures

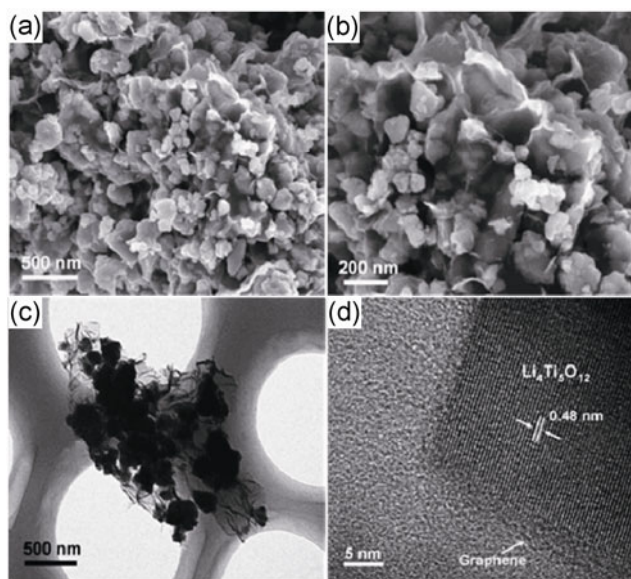


Figure 2 (a) and (b) SEM images of G-LTO nanocomposite at different magnifications. (c) TEM and (d) HR-TEM images of G-LTO nanocomposite.

that LTO particles immobilized on the graphene layers have small size and high distribution. Such a structure should facilitate rapid electron transport because of the graphene sheets inserted among the LTO nanoparticles. Figure 2(d) shows the high resolution TEM (HR-TEM) image of the G-LTO nanocomposite. It is clearly revealed that the LTO particles are firmly attached to the graphene nanosheets. The LTO lattice fringe spacing of 0.48 nm is in good agreement with the distance between the (111) planes of spinel LTO. Furthermore, the well-distributed LTO particles also prevent any serious stacking of the graphene sheets. N_2 adsorption measurements revealed that the G-LTO nanocomposite shows a higher Brunauer-Emmett-Teller (BET) specific surface area (about $18 \text{ m}^2 \cdot \text{g}^{-1}$) than that of pure LTO ($5 \text{ m}^2 \cdot \text{g}^{-1}$).

The G-LTO nanocomposite was first investigated as the anode for LIBs using half-cell performance tests in the potential range 1.0–2.5 V vs. Li/Li⁺ to examine the effectiveness of graphene sheets in improving the electrochemical performance of the hybrid material. The charge-discharge behaviors of G-LTO nanocomposite and pure LTO at different rates are shown in Figs. 3(a) and 3(b). The G-LTO electrode exhibited high discharge capacities of 207, 190, 176, 156, 143, and 123 $\text{mA} \cdot \text{h} \cdot \text{g}^{-1}$ at rates of 0.3, 0.5, 1, 5, 10 and 20 C, respectively, whereas pure LTO showed discharge

capacities of 166, 155, and 75 mA·h·g⁻¹ at 0.5, 1, and 5 C, respectively, with no clear discharge voltage plateau at 10 C rate. Moreover, the Coulombic efficiencies of the G–LTO composite were close to 100%. Compared with the discharge capacity at 1 C, the G–LTO hybrid yield retained 88.8% capacity at 5 C and 81.2% at 10 C (Fig. 3(d)), much higher than the corresponding values for pure LTO (45.9% at 5 C and 14.3% at 10 C), respectively. It is worth noting that at rates of 0.3, 0.5, and 1 C, the G–LTO hybrid delivers ultrahigh capacities which are superior to the theoretical value of 175 mA·h·g⁻¹ for pure LTO. These excellent reversible capacities suggest that the total specific capacity of the G–LTO nanocomposite benefits from a synergistic effect between LTO and graphene. Recently, Hu et al. have shown that the incorporation of a very low weight percentage of graphene (~2 wt.%) can effectively boost the capacity of various Li-ion battery electrode materials beyond the theoretical capacity [48]. It was reported that the reaction of lithium ions with the graphene sheets was responsible for the extra capacity contribution. Thus, the effective specific capacity for

the G–LTO is given by the following equation

$$C_1 = C_L \times 0.964 + C_G \times 0.036 \quad (1)$$

where C_1 is the overall specific capacity of the G–LTO composite, C_L is the specific capacity of LTO, and C_G is the specific capacity of graphene. According to the thermogravimetric analysis, the weight percentages of LTO and graphene are 96.4 wt.% and 3.6 wt.%, respectively, so these factors are employed in the calculation using Eq. 1. Take the capacity of G–LTO at 0.3 C for example. Note that, graphene sheets have been reported to demonstrate a high reversible Li⁺ ion storage capacity of up to 1,100 mA·h·g⁻¹ and LTO is expected to give theoretical capacity of 175 mA·h·g⁻¹ at the low rate of 0.3 C [49]. The calculated specific capacity using Eq. 1 is 208 mA·h·g⁻¹, consistent with the experimental value of 207 mA·h·g⁻¹. Figure 3(c) shows the rate capabilities of the G–LTO nanocomposite and pure LTO at different rates. With increasing discharge rate, the rate capabilities of the G–LTO electrode exhibit a much slower reduction than the pure LTO electrode and a significantly improved rate capability

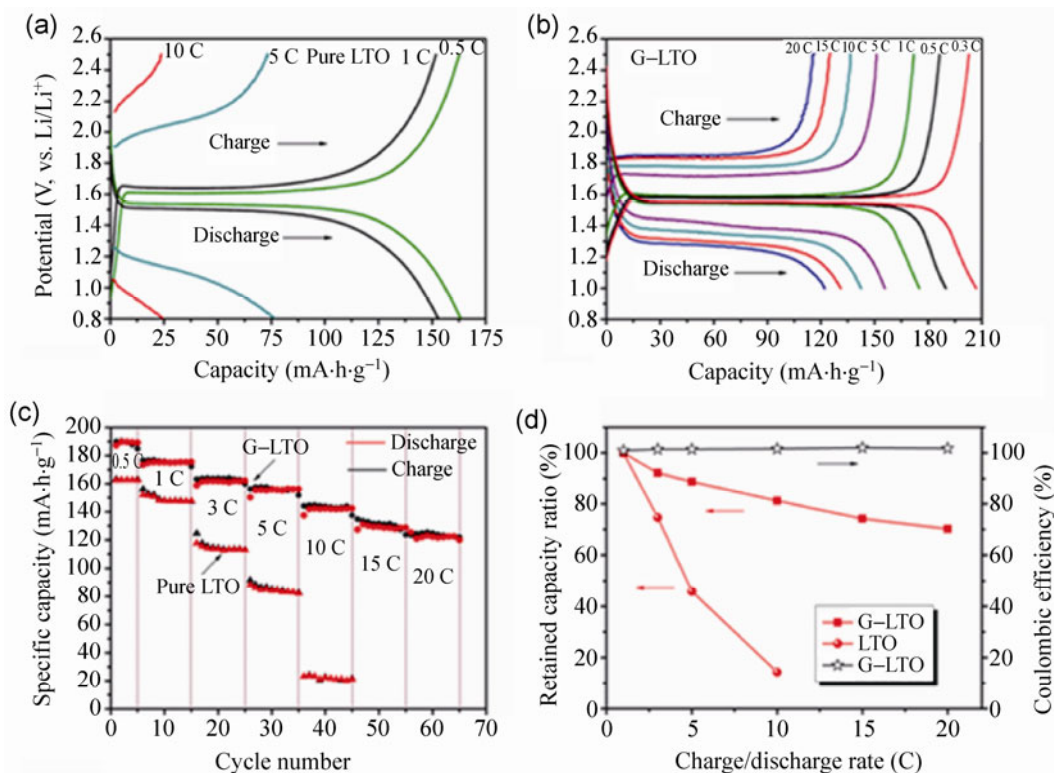


Figure 3 (a) and (b) capacity–voltage profiles for pure LTO and G–LTO nanocomposite. (c) The rate capabilities of G–LTO nanocomposite and pure LTO at different rates. (d) Retained discharge capacity ratio of the G–LTO nanocomposite, pure LTO, and Coulombic efficiencies at various charge–discharge rates of the G–LTO nanocomposite.

was clearly achieved for G–LTO nanocomposite. From the cycling performance shown in Fig. S3 (in the ESM), we can see that G–LTO nanocomposite also exhibits a stable cycle performance at 20 C with a 93% retention of capacity compared with the first discharge capacity of $123 \text{ mA}\cdot\text{h}\cdot\text{g}^{-1}$ after 300 charge–discharge cycles. The cyclic voltammetry (CV) curves of G–LTO and pure LTO were carried out within a potential window of 0.8–2.5 V (vs. Li/Li⁺). As shown in Fig. S4 (in the ESM), the G–LTO shows sharper and well-resolved CV curves compared to the pure LTO. Figure S5 (in the ESM) shows SEM images of the G–LTO electrodes taken before and after 100 charge–discharge cycles: The G–LTO remained uniformly distributed after 100 cycles. Moreover, It can be seen that because of the formation of a SEI film on the surface of G–LTO electrodes, the LTO particles become more smooth [50].

Electrochemical impedance spectra (EIS) of the G–LTO and pure LTO electrodes were measured. The Nyquist plot of the G–LTO nanocomposite (Fig. S6 in the ESM) shows a depressed semicircle in the high frequency region. The impedance analysis results are given in Table S1 (in the ESM). The values of charge transfer resistance (R_{ct}) and the resistance of the

electrolyte (R_s) for the G–LTO composite are 62.7 and 3.5Ω respectively, much lower than the corresponding values of 216.5 and 4.8Ω for the pure LTO. Moreover, compared with the pure LTO, the exchange current density ($i_0 = RT/nFR_{ct}$) [51] value of the G–LTO electrode is much higher. These results further prove that the presence of the graphene network in the G–LTO not only improves the electron transfer kinetics of the insulating LTO but also enhances the accessibility of the electrolyte to the LTO surface, as a result of the fast ion pathways of the graphene network. Therefore, the high energy and rate performance of the G–LTO nanocomposite can be attributed to: (1) the enhanced electrical conductivity due to the inserted graphene electrical network; (2) fast ion and electron pathways due to graphene sheets hindering LTO agglomeration; and (3) an additional EDLC capacity contribution due to the graphene spacer.

2.2 Positive electrode materials

In our previous works [43], a three-dimensional porous G–SU material (shown in Fig. 4(a)) was successfully synthesized by a simple and green process. HR-TEM images of the G–SU hybrid in Figs. 4(b) and S7 (in

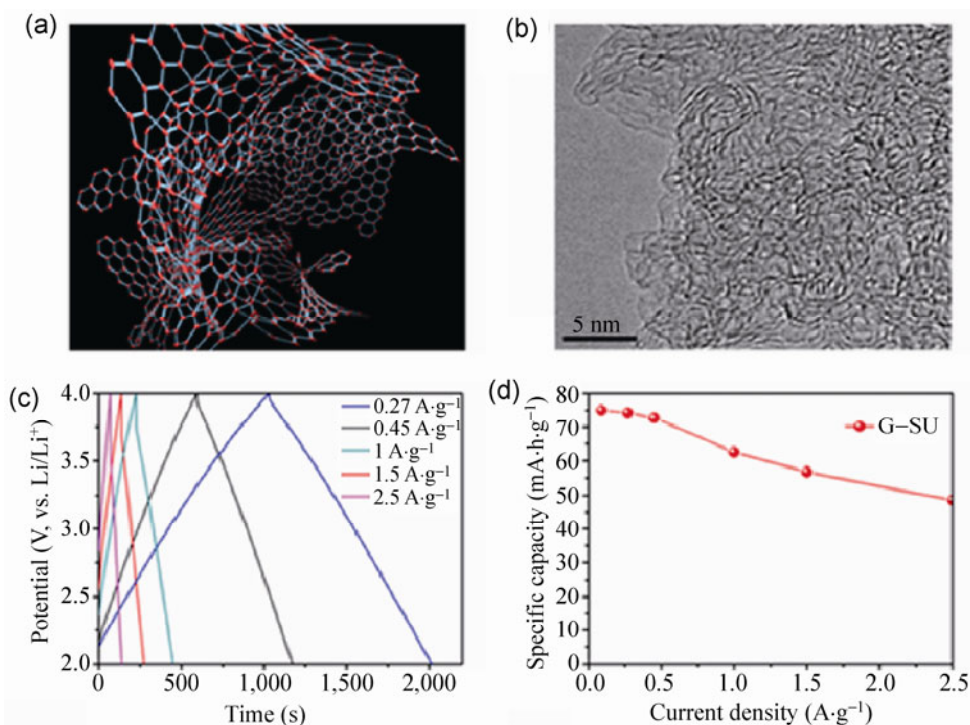


Figure 4 (a) The structure of the G–SU carbon material. (b) HR-TEM image of the G–SU hybrid. (c) Galvanostatic charge–discharge curves of the G–SU hybrid at different current densities. (d) Specific capacities of the G–SU hybrid for each current density.

the ESM) indicate that abundant mesopores are surrounded by highly wrinkled carbon sheets, which contribute to a high BET surface area of $3,355 \text{ m}^2\cdot\text{g}^{-1}$. The electrochemical performance of the porous G–SU hybrid was measured using symmetrical supercapacitor cells with 1 M LiPF_6 electrolyte in the potential range 2–4 V. Figure 4(c) shows the galvanostatic charge–discharge curves of the G–SU hybrid at current densities from 1 to $2.5 \text{ A}\cdot\text{g}^{-1}$. All the curves are highly symmetrical. The specific capacities of the G–SU hybrid were in the range $75\text{--}48 \text{ mA}\cdot\text{h}\cdot\text{g}^{-1}$ for current densities from 1 to $2.5 \text{ A}\cdot\text{g}^{-1}$, as shown in Fig. 4(d). The CV curves of the G–SU half-cell in 1 M LiPF_6 electrolyte (Fig. S8 in the ESM) exhibit nearly rectangular curves over the potential range 2.0–4.0 V at different voltage scan rates ($5\text{--}20 \text{ mV}\cdot\text{s}^{-1}$), also indicating an excellent rate performance. These results suggest that the porous G–SU hybrid could be used as an excellent cathode material for Li-ion hybrid supercapacitors.

2.3 Li-ion hybrid supercapacitors

Since both negative and positive electrode materials demonstrated excellent performance individually, a

hybrid supercapacitor device was then designed and successfully fabricated, using the high energy density G–LTO nanocomposite as the negative electrode and the fast power capability porous G–SU hybrid material as the positive electrode. The mass of the two electrodes must be adjusted to equalize the capacity according to the principle $Q_+ = Q_-$ [15, 52]. Because the specific capacity Q_{sp} is commonly measured and used for electrochemical performance tests, the mass balancing can be expressed as $m_+/m_- = Q_{\text{sp-}}/Q_{\text{sp+}}$ by following the relationship $Q = m \cdot Q_{\text{sp}}$. Based on the data above for the half-cells, the capacity of the G–LTO anode was chosen as $143 \text{ mA}\cdot\text{h}\cdot\text{g}^{-1}$ (10 C) as its typical rate performance for the hybrid supercapacitor, and the practical capacity of the porous G–SU cathode was selected as $48 \text{ mA}\cdot\text{h}\cdot\text{g}^{-1}$ ($2.5 \text{ A}\cdot\text{g}^{-1}$) as its stable capacity value over a wide current density range. Thus, in theory, the mass ratio of the two electrodes in a full-cell hybrid supercapacitor should be $m_{\text{positive}}/m_{\text{negative}} = 2.9$. Figure 5(a) illustrates the experimental relationship between the mass ratio and energy density at the selected rate of 2 C. The maximum value of the specific capacity of the hybrid supercapacitor was observed at

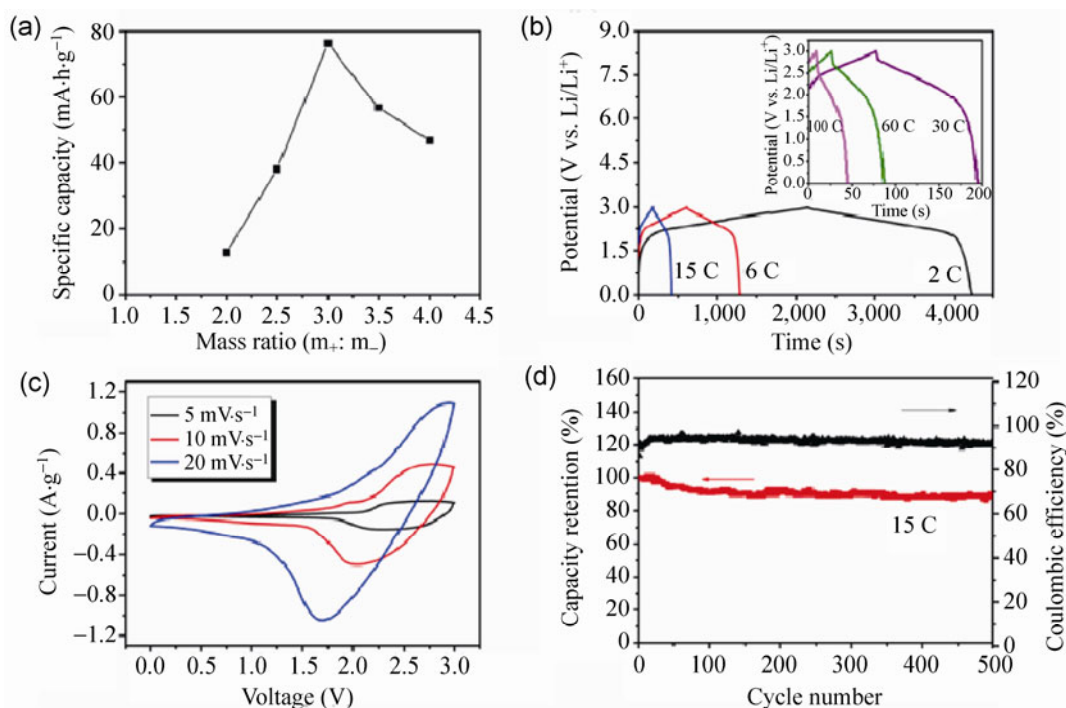


Figure 5 (a) The relationship between mass ratio and energy density at 2 C based on the total active material mass of both electrodes. (b) Galvanostatic charge–discharge curves of the G–LTO//G–SU hybrid supercapacitor at various rates over a potential range of 0–3 V. (c) CV curves of the G–LTO//G–SU hybrid supercapacitor at various rates of 5, 10, $20 \text{ mV}\cdot\text{s}^{-1}$. (d) Cycle stability of the G–LTO//G–SU hybrid supercapacitor for 500 cycles at 15 C.

a mass ratio of $m_{\text{positive}}/m_{\text{negative}} = 3:1$, which is close to the theoretical value. Figure 5(b) shows the galvanostatic charge–discharge curves of the G–LTO//G–SU hybrid supercapacitor over a potential range of 0–3 V. The charge plot demonstrated a rapid increase in potential with time in the early stages, which led to a small amount of capacity data. Then, until the negative electrode potential reached the operating voltage of the LTO in the G–LTO nanocomposite, the charge plot exhibited a lower slope than in the early stages, resulting in a high energy density storage. So the full-cell potential plot showed the typical characteristics of a Li-ion hybrid supercapacitor. Figure 5(c) shows the CV curves at various scan rates. Because of the synergistic effects of different Li-ion storage mechanisms, the G–LTO//G–SU hybrid supercapacitor demonstrates a non-rectangular shape. Additionally, Fig. S9 (in the ESM) shows the small equivalent series resistance of our hybrid supercapacitor. The cycle performance of the G–LTO//G–SU hybrid supercapacitor has a long-term electrochemical stability as shown in Fig. 5(d). It also exhibits an excellent capacity retention of 87% after 500 cycles at 15 C, with high Coulombic efficiency of $\sim 94\%$ during cycles. Moreover, a high first Coulombic efficiency of $\sim 86\%$ was also demonstrated.

The energy density (E) of our Li-ion hybrid supercapacitor was calculated by integrating the Q – V graph area during the discharge process [53]. The power density was calculated using the equation: $P = E/t$,

where t stands for the discharge time. Figure 6(a) shows the Ragone plots of our Li-ion hybrid supercapacitor in the voltage range of 0–3 V. Compared with the conventional symmetrical supercapacitors based on AC or RGO, such as AC/Na₂SO₄/AC supercapacitors ($< 10 \text{ Wh}\cdot\text{kg}^{-1}$) [54–56], RGO/KOH/RGO supercapacitors ($9.1 \text{ Wh}\cdot\text{kg}^{-1}$) [57], and AC/LiPF₆/AC supercapacitors ($< 20 \text{ Wh}\cdot\text{kg}^{-1}$) [58], the G–LTO//G–SU hybrid supercapacitor shows a much higher energy density of $95 \text{ Wh}\cdot\text{kg}^{-1}$ at a power density of $45 \text{ W}\cdot\text{kg}^{-1}$, and still retains an energy density of $32 \text{ Wh}\cdot\text{kg}^{-1}$ at a high power density of $3,000 \text{ W}\cdot\text{kg}^{-1}$. Moreover, our G–LTO//G–SU hybrid supercapacitor also shows significantly improved high power rates compared with the LTO//G–SU device fabricated using pure LTO as the negative electrode material. Because commercial packaged batteries generally contain about 30 wt.% of active material, a factor of 3 is frequently used to extrapolate the energy or power of a device based on the performance of the material itself [59, 60]. Figure 6(b) shows the Ragone plots of the packaged G–LTO//G–SU hybrid supercapacitor. The energy of the G–LTO//G–SU hybrid supercapacitor is highly competitive to typical commercial electrochemical capacitors and the power density of the G–LTO//G–SU is also faster than commercial LIBs.

These results indicate that graphene plays key roles in improving the electrochemical performance of both electrodes, leading to the excellent performance of the final hybrid supercapacitor device. The morphology

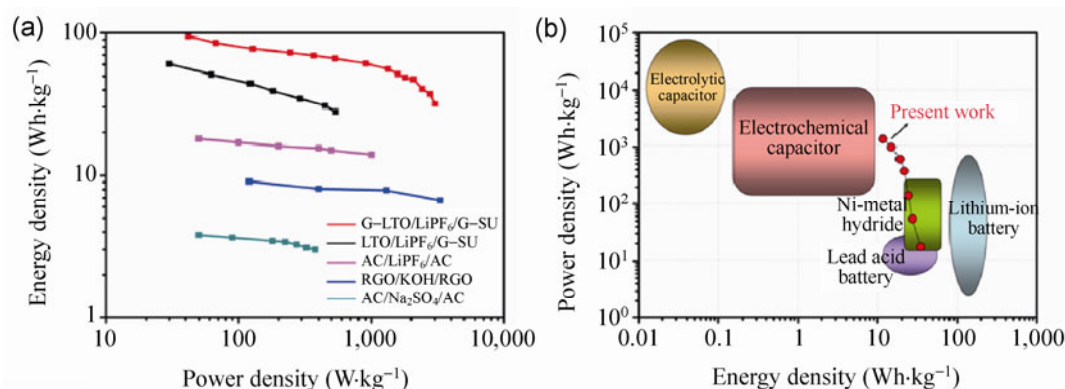


Figure 6 (a) Ragone plots for the G–LTO/LiPF₆/G–SU hybrid supercapacitor based on the total active material mass of both electrodes in comparison to the LTO/LiPF₆/G–SU hybrid supercapacitor and some symmetric supercapacitors reported in the literature, namely activated carbon (AC)/NaSO₄/AC [54], reduced graphene oxide (RGO)/KOH/RGO [57], and activated carbon AC/LiPF₆/AC [58]. (b) Ragone plots for the packaged G–LTO/LiPF₆/G–SU hybrid supercapacitor and two typical electrical energy storage devices.

of the graphene conducting network present in the G–LTO hybrid can not only improve the electrical conductivity but also probably shorten the ion diffusion length to the surface of the LTO particles. The graphene sheets are separated by the LTO particles decreasing the agglomeration, and this also provides additional EDLC, contributing to the improved capacity of the G–LTO hybrid. The superior performance of G–SU as a positive electrode material compared with the conventional AC material, also contributes to the overall excellent performance of the hybrid supercapacitor.

3 Conclusion

We have demonstrated an advanced hybrid supercapacitor G–LTO//G–SU consisting of a G–LTO anode and a three-dimensional porous G–SU cathode giving both high energy and power densities. Graphene plays a key role in the overall significantly improved performance, due to its well distributed and highly electrical conducting network as well as its high surface area. The encouraging results presented here demonstrate that hybrid supercapacitor systems based on graphene could be a promising energy storage system affording both high energy and power densities.

4 Experimental

4.1 Preparation of G–LTO nanocomposite

A series of graphene-inserted LTO composites with different loadings of GO were synthesized and the optimized product, denoted G–LTO with 3.6 wt.% graphene (measured by thermogravimetric analysis (TGA)), was used as an example to demonstrate the procedure. The G–LTO nanocomposite was prepared by solvothermal and heat treatment, as illustrated in Scheme 1. Nanosized LTO was first obtained by ball milling treatment of commercial $\text{Li}_4\text{Ti}_5\text{O}_{12}$ (diameter $\sim 2 \mu\text{m}$, > 99% purity, Fig. S10(a) in the ESM). Graphene oxide (GO, Fig. S10(b) in the ESM) was synthesized using a modified Hummers method [61]. For the fabrication of G–LTO nanoparticles, a homogeneous aqueous solution of GO (2 mg/mL) was added to an ethanol suspension of nanosized LTO to give a 1:8

weight ratio of GO to LTO and the mixture vigorously stirred for 12 h the ethanol/water volume ratio in the colloidal suspension was about 1:2. The intermediate product was transferred into a Teflon-lined stainless steel autoclave, which was then heated to 150 °C and the temperature maintained for 12 h. After the solvothermal reaction, the almost transparent nature of the supernatant solution indicated that graphene sheets were incorporated into the precipitated nanocomposite. The resulting precipitate was separated by filtration, washed with deionized water, and heated to 500 °C for 4 h under a mixed gas flow (5% H_2 and 95% Ar). Finally, a dark grey powder product was obtained.

4.2 Synthesis of G–SU hybrid

The porous graphene–sucrose carbon composite was prepared as described in our previous report [43]. Briefly, a hydrothermal GO/sucrose dispersion with a 1:24 weight ratio was transferred into a sealed 100 mL Teflon-lined autoclave, which was heated to 200 °C for 12 h. The precipitate was then washed and dried. A mixture of the product and KOH (KOH/hydrothermal product = 4) was then heated to 800 °C for 1 h under a mixed gas flow (5% H_2 and 95% Ar). The resulting solid was washed with 0.1 M HCl and dried in vacuum at 120 °C for 24 h to obtain the final product.

4.3 Characterization

XRD measurements were performed on a Rigaku D/Max-2500 diffractometer with $\text{Cu K}\alpha$ radiation. SEM was conducted using a LEO 1530 VP field emission scanning electron microscope with acceleration voltage of 10 kV. TEM was carried out using a JEOL TEM-2100 electron microscope. Raman spectra were recorded with a LabRAM HR Raman spectrometer using laser excitation at 514.5 nm. Combustion elemental analysis using a Vario Micro cube, (Elementar, Germany) and inductively coupled plasma–mass spectrometry (X7 Series, Thermo Electron Corporation, USA) were carried out to determine the C, H, O, Li, and Ti content. Thermogravimetric (TG) analysis was carried out from 30 °C to 950 °C at a heating rate of 10 °C·min⁻¹ in air. XPS was carried out using an AXIS HIS 165 spectrometer with a monochromatized Al $\text{K}\alpha$ X-ray source (1486.71 eV). The surface area was calculated

by the BET method. The electrical conductivity of the negative electrode material G–LTO was measured by the following method. G–LTO was mixed with 10 wt.% polytetrafluoroethylene (PTFE, solid powder, Dupont) as a binder, and homogenized in an agate mortar. Then it was rolled into 80–100 μm thickness sheets and pressed at 20 MPa and finally cut into $3 \times 1 \text{ cm}^2$ sheets. These were coated with silver conductive adhesives on both sides and tested using a multimeter. The conductivity of the film was calculated using the formula $\lambda = L/(R_x W d)$, where λ is the electrical conductivity of sample, and L , W , and d are the length, width and thickness of the sheet respectively, and R_x is the resistance of the sheet as measured by the multimeter.

4.4 Electrochemical measurements

The electrochemical performance of the G–LTO anode, G–SU cathode and G–LTO//G–SU hybrid supercapacitor was evaluated using two-electrode cells following the standard industry procedure. For fabrication of the G–LTO electrodes, the electroactive material, carbon black, and polyvinylidene fluoride (PVDF) with *N*-methylpyrrolidone (NMP) as solvent were mixed with a 85:10:5 mass ratio, then coated onto a piece of copper foil and rolled into 150 μm thickness sheets. After drying under vacuum at 150 $^\circ\text{C}$ for 6 h, the foil was pressed and punched into 12 mm diameter disks. Comparable half-cells containing pure LTO were assembled and tested under the exact same conditions. The G–SU half-cell was fabricated by mixing 90 wt.% active material and 10 wt.% PTFE with ethanol as solvent, followed by rolling into 80–100 μm thickness sheets and punching into 12 mm diameter disks. The disks were hot pressed onto conductive carbon-coated aluminum foils. The as-prepared G–LTO anode and G–SU cathode disks were first assembled as half-cells using coin-type cells. Both anode and cathode used lithium metal foil as the counter electrode, and 1 M LiPF_6 dissolved in ethylene carbonate (EC), dimethyl carbonate (DMC), and diethyl carbonate (DEC) with a volume ratio (1:1:1) was used as the electrolyte. The hybrid supercapacitor was assembled using the same coin-type cell and electrolyte. The optimized mass ratio of G–SU:G–LTO was 3. Comparable full-cells containing a G–SU anode with a pure LTO anode

with a mass ratio of 3 were assembled and tested under the same conditions. EIS and CV were conducted using an Autolab (Metrohm) Analyzer. Galvanostatic charge–discharge measurements were performed using a LAND CT2001A model test system. All the electrochemical tests were carried out at room temperature.

Acknowledgements

The authors gratefully acknowledge financial support from Ministry of Science and Technology of the People's Republic of China (MoST) (Grants Nos. 2012CB933401 and 2011DFB50300), and National Natural Science Foundation of China (NSFC) (Grants Nos. 50933003 and 51273093).

Electronic Supplementary Material: Supplementary material (TG curve of G–LTO composite, XPS spectra (C 1s, O 1s, and Ti 2p) of the G–LTO nanocomposite, specific capacity and Coulombic efficiency of the G–LTO, electrochemical impedance spectra of the pure LTO and G–LTO nanocomposite electrodes, table of impedance parameters of LTO and G–LTO nanocomposite electrodes, high-magnification TEM image of the G–SU hybrid, and SEM images of GO and pure LTO) is available in the online version of this article at <http://dx.doi.org/10.1007/s12274-013-0334-6>.

References

- [1] Armand, M.; Tarascon, J. M. Building better batteries. *Nature* **2008**, *451*, 652–657.
- [2] Miller, J. R.; Simon, P. Electrochemical capacitors for energy management. *Science* **2008**, *321*, 651–652.
- [3] Simon, P.; Gogotsi, Y. Materials for electrochemical capacitors. *Nat. Mater.* **2008**, *7*, 845–854.
- [4] Tarascon, J. M.; Armand, M. Issues and challenges facing rechargeable lithium batteries. *Nature* **2001**, *414*, 359–367.
- [5] Du Pasquier, A.; Plitz, I.; Menocal, S.; Amatucci, G. A comparative study of Li-ion battery, supercapacitor and nonaqueous asymmetric hybrid devices for automotive applications. *J. Power Sources* **2003**, *115*, 171–178.
- [6] Pasquier, A. D.; Plitz, I.; Gural, J.; Badway, F.; Amatucci, G. G. Power-ion battery: Bridging the gap between Li-ion and supercapacitor chemistries. *J. Power Sources* **2004**, *136*, 160–170.

- [7] Liu, C.; Li, F.; Ma, L. P.; Cheng, H. M. Advanced materials for energy storage. *Adv. Mater.* **2010**, *22*, E28–E62.
- [8] Naoi, K.; Ishimoto, S.; Miyamoto, J. I.; Naoi, W. Second generation “nanohybrid supercapacitor”: Evolution of capacitive energy storage devices. *Energy Environ. Sci.* **2012**, *5*, 9363–9373.
- [9] Burke, A. R&D considerations for the performance and application of electrochemical capacitors. *Electrochim. Acta* **2007**, *53*, 1083–1091.
- [10] Chen, F.; Li, R. G.; Hou, M.; Liu, L.; Wang, R.; Deng, Z. H. Preparation and characterization of ramsdellite $\text{Li}_2\text{Ti}_3\text{O}_7$ as an anode material for asymmetric supercapacitors. *Electrochim. Acta* **2005**, *51*, 61–65.
- [11] Zheng, J. P. The limitations of energy density of battery/double-layer capacitor asymmetric cells. *J. Electrochem. Soc.* **2003**, *150*, A484–A492.
- [12] Wang, Y. G.; Xia, Y. Y. A new concept hybrid electrochemical supercapacitor: Carbon/ LiMn_2O_4 aqueous system. *Electrochem. Commun.* **2005**, *7*, 1138–1142.
- [13] Pell, W. G.; Conway, B. E. Peculiarities and requirements of asymmetric capacitor devices based on combination of capacitor and battery-type electrodes. *J. Power Sources* **2004**, *136*, 334–345.
- [14] Amatucci, G. G.; Badway, F.; Du Pasquier, A.; Zheng, T. An asymmetric hybrid nonaqueous energy storage cell. *J. Electrochem. Soc.* **2001**, *148*, A930–A939.
- [15] Ni, J. F.; Yang, L. X.; Wang, H. B.; Gao, L. J. A high-performance hybrid supercapacitor with $\text{Li}_4\text{Ti}_5\text{O}_{12}$ -C nanocomposite prepared by *in situ* and *ex situ* carbon modification. *J. Solid State Electrochem.* **2012**, *16*, 2791–2796.
- [16] Wang, Q.; Wen, Z. H.; Li, J. H. A hybrid supercapacitor fabricated with a carbon nanotube cathode and a TiO_2 -B nanowire anode. *Adv. Funct. Mater.* **2006**, *16*, 2141–2146.
- [17] Cericola, D.; Novák, P.; Wokaun, A.; Kötz, R. Hybridization of electrochemical capacitors and rechargeable batteries: An experimental analysis of the different possible approaches utilizing activated carbon, $\text{Li}_4\text{Ti}_5\text{O}_{12}$ and LiMn_2O_4 . *J. Power Sources* **2011**, *196*, 10305–10313.
- [18] Li, H. Q.; Cheng, L.; Xia, Y. Y. A hybrid electrochemical supercapacitor based on a 5 V Li-ion battery cathode and active carbon. *Electrochem. Solid-State Lett.* **2005**, *8*, A433–A436.
- [19] Chen, P. C.; Shen, G. Z.; Shi, Y.; Chen, H. T.; Zhou, C. W. Preparation and characterization of flexible asymmetric supercapacitors based on transition-metal-oxide nanowire/single-walled carbon nanotube hybrid thin-film electrodes. *ACS Nano* **2010**, *4*, 4403–4411.
- [20] Aricò, A. S.; Bruce, P.; Scrosati, B.; Tarascon, J. M.; van Schalkwijk, W. Nanostructured materials for advanced energy conversion and storage devices. *Nat. Mater.* **2005**, *4*, 366–377.
- [21] Chen, Z.; Augustyn, V.; Wen, J.; Zhang, Y. W.; Shen, M. Q.; Dunn, B.; Lu, Y. F. High-performance supercapacitors based on intertwined CNT/ V_2O_5 nanowire nanocomposites. *Adv. Mater.* **2011**, *23*, 791–795.
- [22] Fan, Z. J.; Yan, J.; Zhi, L. J.; Zhang, Q.; Wei, T.; Feng, J.; Zhang, M. L.; Qian, W. Z.; Wei, F. A three-dimensional carbon nanotube/graphene sandwich and its application as electrode in supercapacitors. *Adv. Mater.* **2010**, *22*, 3723–3728.
- [23] Armstrong, G.; Armstrong, A. R.; Bruce, P. G.; Reale, P.; Scrosati, B. $\text{TiO}_2(\text{B})$ Nanowires as an improved anode material for lithium-ion batteries containing LiFePO_4 or $\text{LiNi}_{0.5}\text{Mn}_{1.5}\text{O}_4$ cathodes and a polymer electrolyte. *Adv. Mater.* **2006**, *18*, 2597–2600.
- [24] Winter, M.; Besenhard, J. O. Electrochemical lithiation of tin and tin-based intermetallics and composites. *Electrochim. Acta* **1999**, *45*, 31–50.
- [25] Mukaibo, H.; Osaka, T.; Reale, P.; Panero, S.; Scrosati, B.; Wachtler, M. Optimized Sn/SnSb lithium storage materials. *J. Power Sources* **2004**, *132*, 225–228.
- [26] Bruce, P. G.; Scrosati, B.; Tarascon, J. M. Nanomaterials for rechargeable lithium batteries. *Angew. Chem. Int. Ed.* **2008**, *47*, 2930–2946.
- [27] Naoi, K.; Simon, P. New materials and new configurations for advanced electrochemical capacitors. *Interface* **2008**, *17*, 34–37.
- [28] Naoi, K. “Nanohybrid capacitor”: The next generation electrochemical capacitors. *Fuel Cells* **2010**, *10*, 8254–833.
- [29] Park, K. S.; Benayad, A.; Kang, D. J.; Doo, S. G. Nitridation-driven conductive $\text{Li}_4\text{Ti}_5\text{O}_{12}$ for lithium ion batteries. *J. Am. Chem. Soc.* **2008**, *130*, 14930–14931.
- [30] Wang, Y. G.; Liu, H. M.; Wang, K. X.; Eiji, H.; Wang, Y. R.; Zhou, H. S. Synthesis and electrochemical performance of nano-sized $\text{Li}_4\text{Ti}_5\text{O}_{12}$ with double surface modification of Ti(III) and carbon. *J. Mater. Chem.* **2009**, *19*, 6789–6795.
- [31] Sorensen, E. M.; Barry, S. J.; Jung, H. K.; Rondinelli, J. M.; Vaughey, J. T.; Poeppelmeier, K. R. Three-dimensionally ordered macroporous $\text{Li}_4\text{Ti}_5\text{O}_{12}$: Effect of wall structure on electrochemical properties. *Chem. Mater.* **2005**, *18*, 482–489.
- [32] Yi, T. F.; Jiang, L. J.; Liu, J.; Ye, M. F.; Fang, H. B.; Zhou, A. N.; Shu, J. Structure and physical properties of $\text{Li}_4\text{Ti}_5\text{O}_{12}$ synthesized at deoxidation atmosphere. *Ionics* **2011**, *17*, 799–803.
- [33] Cheng, L.; Yan, J.; Zhu, G. N.; Luo, J. Y.; Wang, C. X.; Xia, Y. Y. General synthesis of carbon-coated nanostructure $\text{Li}_4\text{Ti}_5\text{O}_{12}$ as a high rate electrode material for Li-ion intercalation. *J. Mater. Chem.* **2010**, *20*, 595–602.
- [34] Wang, G. J.; Gao, J.; Fu, L. J.; Zhao, N. H.; Wu, Y. P.; Takamura, T. Preparation and characteristic of carbon-coated $\text{Li}_4\text{Ti}_5\text{O}_{12}$ anode material. *J. Power Sources* **2007**, *174*, 1109–1112.

- [35] Jiang, C.; Ichihara, M.; Honma, I.; Zhou, H. S. Effect of particle dispersion on high rate performance of nano-sized $\text{Li}_4\text{Ti}_5\text{O}_{12}$ anode. *Electrochim. Acta* **2007**, *52*, 6470–6475.
- [36] Huang, S. H.; Wen, Z. Y.; Zhu, X. J.; Lin, Z. X. Effects of dopant on the electrochemical performance of $\text{Li}_4\text{Ti}_5\text{O}_{12}$ as electrode material for lithium ion batteries. *J. Power Sources* **2007**, *165*, 408–412.
- [37] Huang, S. H.; Wen, Z. Y.; Zhang, J. C.; Yang, X. L. Improving the electrochemical performance of $\text{Li}_4\text{Ti}_5\text{O}_{12}/\text{Ag}$ composite by an electroless deposition method. *Electrochim. Acta* **2007**, *52*, 3704–3708.
- [38] Li, J. R.; Tang, Z. L.; Zhang, Z. T. Controllable formation and electrochemical properties of one-dimensional nanostructured spinel $\text{Li}_4\text{Ti}_5\text{O}_{12}$. *Electrochem. Commun.* **2005**, *7*, 894–899.
- [39] Zheng, S. W.; Xu, Y. L.; Zhao, C. J.; Liu, H. K.; Qian, X. Z.; Wang, J. H. Synthesis of nano-sized $\text{Li}_4\text{Ti}_5\text{O}_{12}/\text{C}$ composite anode material with excellent high-rate performance. *Mater. Lett.* **2012**, *68*, 32–35.
- [40] Li, X.; Qu, M. Z.; Huai, Y. J.; Yu, Z. L. Preparation and electrochemical performance of $\text{Li}_4\text{Ti}_5\text{O}_{12}/\text{carbon}/\text{carbon}$ nano-tubes for lithium ion battery. *Electrochim. Acta* **2010**, *55*, 2978–2982.
- [41] Wang, Y.; Shi, Z. Q.; Huang, Y.; Ma, Y. F.; Wang, C. Y.; Chen, M. M.; Chen, Y. S. Supercapacitor devices based on graphene materials. *J. Phys. Chem. C* **2009**, *113*, 13103–13107.
- [42] Wang, Y.; Wu, Y. P.; Huang, Y.; Zhang, F.; Yang, X.; Ma, Y. F.; Chen, Y. S. Preventing graphene sheets from restacking for its high capacitance performance. *J. Phys. Chem. C* **2011**, *115*, 23192–23197.
- [43] Zhang, L.; Zhang, F.; Yang, X.; Long, G. K.; Wu, Y. P.; Zhang, T. F.; Leng, K.; Huang, Y.; Ma, Y. F.; Chen, Y. S. Porous 3D graphene-based bulk materials with exceptional high surface area and excellent conductivity for supercapacitors. *Sci. Rep.* **2013**, *3*, 1408–1417.
- [44] Li, C.; Shi, G. Three-dimensional graphene architectures. *Nanoscale* **2012**, *4*, 5549–5563.
- [45] Prossini, P. P.; Mancini, R.; Petrucci, L.; Contini, V.; Villano, P. $\text{Li}_4\text{Ti}_5\text{O}_{12}$ as anode in all-solid-state, plastic, lithium-ion batteries for low-power applications. *Solid State Ionics* **2001**, *144*, 185–192.
- [46] Aldon, L.; Kubiak, P.; Womes, M.; Jumas, J. C.; Olivier-Fourcade, J.; Tirado, J. L.; Corredor, J. I.; Pérez Vicente, C. Chemical and electrochemical Li-insertion into the $\text{Li}_4\text{Ti}_5\text{O}_{12}$ spinel. *Chem. Mater.* **2004**, *16*, 5721–5725.
- [47] Yan, J.; Wei, T.; Shao, B.; Fan, Z. J.; Qian, W. Z.; Zhang, M. L.; Wei, F. Preparation of a graphene nanosheet/polyaniline composite with high specific capacitance. *Carbon* **2010**, *48*, 487–493.
- [48] Hu, L. H.; Wu, F. Y.; Lin, C. T.; Khlobystov, A. N.; Li, L. J. Graphene-modified LiFePO_4 cathode for lithium ion battery beyond theoretical capacity. *Nat. Commun.* **2013**, *4*, 687–1674.
- [49] Pan, D. Y.; Wang, S.; Zhao, B.; Wu, M. H.; Zhang, H. J.; Wang, Y.; Jiao, Z. Li storage properties of disordered graphene nanosheets. *Chem. Mater.* **2009**, *21*, 3136–3142.
- [50] Kitta, M.; Akita, T.; Maeda, Y.; Kohyama, M. Study of surface reaction of spinel $\text{Li}_4\text{Ti}_5\text{O}_{12}$ during the first lithium insertion and extraction processes using atomic force microscopy and analytical transmission electron microscopy. *Langmuir* **2012**, *28*, 12384–12392.
- [51] Wang, G. X.; Wang, B.; Wang, X. L.; Park, J.; Dou, S.; Ahn, H.; Kim, K. Sn/graphene nanocomposite with 3D architecture for enhanced reversible lithium storage in lithium ion batteries. *J. Mater. Chem.* **2009**, *19*, 8378–8384.
- [52] Naoi, K.; Ishimoto, S.; Isobe, Y.; Aoyagi, S. High-rate nanocrystalline $\text{Li}_4\text{Ti}_5\text{O}_{12}$ attached on carbon nano-fibers for hybrid supercapacitors. *J. Power Sources* **2010**, *195*, 6250–6254.
- [53] Tang, Y. F.; Yang, L.; Qiu, Z.; Huang, J. S. Preparation and electrochemical lithium storage of flower-like spinel $\text{Li}_4\text{Ti}_5\text{O}_{12}$ consisting of nanosheets. *Electrochem. Commun.* **2008**, *10*, 1513–1516.
- [54] Zheng, C.; Qi, L.; Yoshio, M.; Wang, H. Y. Cooperation of micro- and meso-porous carbon electrode materials in electric double-layer capacitors. *J. Power Sources* **2010**, *195*, 4406–4409.
- [55] Qu, Q. T.; Li, L.; Tian, S.; Guo, W. L.; Wu, Y. P.; Holze, R. A cheap asymmetric supercapacitor with high energy at high power: Activated carbon// $\text{K}_{0.27}\text{MnO}_2 \cdot 0.6\text{H}_2\text{O}$. *J. Power Sources* **2010**, *195*, 2789–2794.
- [56] Khomenko, V.; Piñero, E. R.; Béguin, F. A new type of high energy asymmetric capacitor with nanoporous carbon electrodes in aqueous electrolyte. *J. Power Sources* **2010**, *195*, 4234–4241.
- [57] Wang, H. L.; Liang, Y. Y.; Mirfakhrai, T.; Chen, Z.; Casalongue, H.; Dai, H. J. Advanced asymmetrical supercapacitors based on graphene hybrid materials. *Nano Res.* **2011**, *4*, 729–736.
- [58] Choi, H. S.; Im, J. H.; Kim, T.; Park, J. H.; Park, C. R. Advanced energy storage device: A hybrid BatCap system consisting of battery-supercapacitor hybrid electrodes based on $\text{Li}_4\text{Ti}_5\text{O}_{12}$ -activated-carbon hybrid nanotubes. *J. Mater. Chem.* **2012**, *22*, 16986–16993.
- [59] Gogotsi, Y.; Simon, P. True performance metrics in electrochemical energy storage. *Science* **2011**, *334*, 917–918.
- [60] Stoller, M. D.; Murali, S.; Quarles, N.; Zhu, Y. W.; Potts, J. R.; Zhu, X. J.; Ha, H. W.; Ruoff, R. S. Activated graphene as a cathode material for Li-ion hybrid supercapacitors. *Phys. Chem. Chem. Phys.* **2012**, *14*, 3388–3391.
- [61] Becerril, H. A.; Mao, J.; Liu, Z. F.; Stoltenberg, R. M.; Bao, Z. N.; Chen, Y. S. Evaluation of solution-processed reduced graphene oxide films as transparent conductors. *ACS Nano* **2008**, *2*, 463–470.